

Critical penetration condition and Ekman suction-extraction mechanism of a sink vortex^{*}

Da-peng TAN[†], Lin LI, Yin-long ZHU, Shuai ZHENG, Zi-chao YIN, Dai-feng LI

College of Mechanical Engineering, Zhejiang University of Technology, Hangzhou 310014, China

[†]E-mail: tandapeng@zjut.edu.cn

Received Apr. 21, 2018; Revision accepted Aug. 2, 2018; Crosschecked Aug. 10, 2018; Published online Sept. 21, 2018

Abstract: The critical penetration condition is an essential component of studies on the mechanism of sink vortex formation. However, the condition and its transition process are unknown. To address this issue, we constructed a Rankine-vortex-based fluid mechanic model, and proposed a Helmholtz-equation-based solution method to acquire the critical penetration condition. The two-phase mass suction-extraction mechanism of the Ekman boundary layer was discussed. Numerical results show that the critical penetration condition is dependent on the initial velocity components; if the initial disturbances are enhanced, the suction-extraction height and Ekman layer thickness increase. A particle image velocimetry (PIV)-based observation experimental platform was developed, and the effectiveness of the proposed method was verified. The vortex core boundary was observed first, so the radius of the vortex core could be acquired precisely.

Key words: Sink vortex; Critical penetration condition; Ekman boundary layer; Suction-extraction mechanism
<https://doi.org/10.1631/jzus.A1800260>

CLC number: O35

1 Introduction

When a fluid drains from a vessel with a drainage outlet, owing to the effects of gravity, Coriolis force, and other external disturbances, a sink vortex with a free surface will appear. If the vortex front-end arrives at the outlet, the central area of the vortex generates a gaseous core, which is the so-called critical state of vortex formation, i.e. vortex penetration (Fig. 1a). The rotation direction of the vortex is random, and depends on the rotating component of the initial disturbing velocity (Tan et al., 2010; Chen YC et al., 2013; Tan and Zhang, 2014; Chen JL et al., 2015; Zhao and Li, 2016; Ghani et al., 2017; Ding et al., 2018).

A sink vortex is not only a common physical phenomenon, but a complex fluid mechanics issue with highly nonlinear features. The sink vortex is relevant to some industry applications, in which the two-phase suction-extraction mechanism of the Ekman boundary layer is the key physical process. Therefore, revealing the variation laws of vortex formation and Ekman suction-extraction has scientific and engineering significance for areas of metallurgy, chemistry, and hydraulics (Tan et al., 2009, 2013, 2017c; Dolan and Oliveira, 2013; Zhao et al., 2017; Ge et al., 2018; Turkyilmazoglu, 2018).

Through the use of classical fluid mechanic methods, the vortex velocity and height distribution on radius direction had been obtained (Lundgren, 1985). With respect to nonlinear flow and surface tension, an upward flow region generated by the Ekman layer at the bottom of the container was observed (Andersen et al., 2003, 2006). According to the above hypothesis, Aboelkassem et al. (2005) and Yokoyama et al. (2012) found that a sink vortex

^{*} Project supported by the National Natural Science Foundation of China (No. 51775501) and the Zhejiang Provincial Natural Science Foundation of China (No. LR16E050001)

 ORCID: Da-peng TAN, <https://orcid.org/0000-0002-6018-9648>

© Zhejiang University and Springer-Verlag GmbH Germany, part of Springer Nature 2018

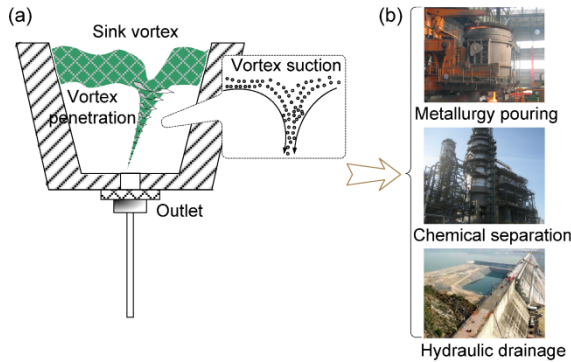


Fig. 1 Free sink vortex and relevant applications

(a) When the rotation energy breaks through the liquid surface tension, the vortex is penetrating; (b) A sink vortex occurs in some industrial processes, such as metallurgy pouring, chemical separation, and hydraulic drainage, and can conduct some negative effects on industrial production

exhibited a two-celled structure with Ekman pumping-upwelling. Lin et al. (2010) identified factors influencing a sink vortex using a water-modeling method. The factors included the initial liquid level, nozzle diameter, and eccentricity. He found that the initial flow field conditions could determine the geometrical scale of a sink vortex. Li et al. (2016) analyzed the key factors affecting free surface vortex formation and found that the Coriolis force had little effect on vortex formation, and the initial tangential disturbance was the main factor.

The above reports show that studies of the sink vortex are very challenging, and the critical penetration condition and mass transfer mechanism remain unknown. Currently, there are no methods for analysing the critical condition of sink vortex formation. However, obtaining the critical condition is necessary to be able to actively control vortex formation in relevant industrial applications (Shi et al., 2011; Peterson and Porfiri, 2012; Zeng et al., 2013, 2014; Li PX et al., 2017; Tan et al., 2017b; Chen and Tan, 2018; Wang et al., 2018). Therefore, in this study we propose a sink vortex modeling method to obtain the critical condition of vortex formation, and reveal the mass transfer laws of Ekman boundary layer suction-extraction.

Our results not only offer theoretical references for future research on fluid dynamic subjects with free interfaces, but can provide technical support and direct guidance for the active control of vortex formation in the engineering areas of metallurgy, chemistry, hydraulics, and petroleum production.

2 Rankine-vortex-based mechanic model

Since the velocity/pressure profiles of sink vortices are similar to those of the Rankine vortex (Tyvand and Haugena, 2005; Aboelkassem and Georgicis, 2007; Wu ZH et al., 2016; Zhang et al., 2017), we set up a mechanical model based on the Rankine vortex to analyze the penetration condition of a sink vortex. The Rankine vortex is a model for a 2D potential vortex, which contains a vortex core and out-of-core flow, and can resolve the matter of velocity singularity on a vortex central point (Fig. 2).

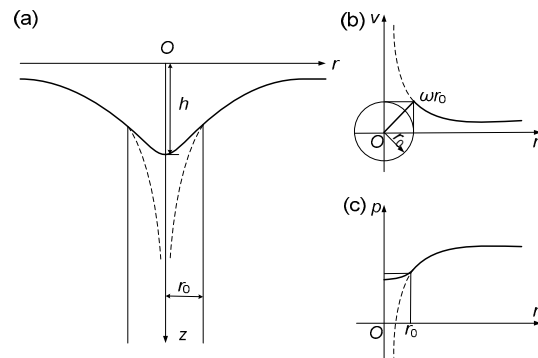


Fig. 2 Theoretical model of a Rankine vortex

(a) The vortex structure comprises a rigid vortex core and out-of-core flow; the core radius is r_0 , and the depth is h ; (b) The velocity distribution contains two segments in accordance with Eq. (1). For the fluid mass point at $r=r_0$, $v_\theta=0$ and $v_z>0$; (c) The pressure distribution also contains two segments, as described in Eq. (5), in which the initial pressure is the sum of atmospheric pressure and potential pressure

In the Euler frame, the velocity of the fluid mass-point is v , and v_r , v_θ , and v_z are the three velocity components (Zheng et al., 2015; Tan et al., 2016c; Ji et al., 2017; Li J et al., 2017). Assuming the radius of the vortex core is r_0 , the vorticity Ω has an even distribution, and the vorticity intensity is Γ , then the core angular velocity is $\omega = \Gamma / (2\pi r_0^2)$. The circular velocity v_θ accords with velocity distribution laws, and the amplitude equals the induced velocity: $v_\theta = \Gamma / (2\pi r) = \omega r_0^2 / r$. If the vortex core is regarded as a cylindrical rigid body, then

$$v_\theta = \begin{cases} \omega r, & r \leq r_0, \\ \omega r_0^2 / r, & r \geq r_0. \end{cases} \quad (1)$$

Supposing the fluid density is ρ and the atmospheric pressure is P_0 , by the Lamb-ГРОМЕКО equation (Tong, 2006), the following expression is obtained:

$$\nabla \left(\frac{p}{\rho} + \frac{1}{2} v^2 - gz \right) = v \times \Omega, \quad (2)$$

where p is the fluid pressure, g is the acceleration due to gravity, and z is the height of the vortex surface. Because the velocity v has an orthogonal relationship to vorticity Ω , it can be described by the stream function ψ :

$$v \times \Omega = \Omega \nabla \psi. \quad (3)$$

Then, Eq. (2) is transformed as

$$\frac{p}{\rho} + \frac{1}{2} v^2 - gz + \int \Omega d\psi = C, \quad (4)$$

where C is the pressure integral constant.

For the following boundary conditions:

$$v|_{r=0} = \Gamma|_{r=0} = 0, \quad z|_{r \rightarrow \infty} = v|_{r \rightarrow \infty} = 0, \quad p|_{r \rightarrow \infty} = P_0,$$

Eq. (4) can be integrated as

$$p(r, z) = \begin{cases} P_0 + \rho gz - \rho r_0^2 \omega^2 \left(1 - \frac{r^2}{2r_0^2} \right), & r \leq r_0, \\ P_0 + \rho gz - \frac{\rho \omega^2 r_0^4}{2r^2}, & r \geq r_0. \end{cases} \quad (5)$$

Apparently, the surface height z has a proportional relationship to ω^2 . If ω reaches the critical value, the vortex will penetrate and generate a gaseous core. If the surface descends continuously with v_z , the following expression is obtained:

$$\begin{cases} p - P_0 - \rho gz + \rho r_0^2 \omega^2 \left(1 - \frac{r^2}{2r_0^2} \right) + \frac{1}{2} v_z^2 \\ \quad = C_1, & r \leq r_0, \\ p - P_0 - \rho gz + \frac{\rho \omega^2 r_0^4}{2r^2} + \frac{1}{2} v_z^2 \\ \quad = C_2, & r \geq r_0. \end{cases} \quad (6)$$

Eq. (6) accords with the Bernoulli equation (Tan et al., 2016a; Wu HP et al., 2016; Huang et al., 2017; Shi and Li, 2018), where $p - P_0$ is the hydrostatic pressure, $\rho r_0^2 \omega^2 (1 - r^2 / (2r_0^2)) + v_z^2 / 2$, $\rho \omega^2 r_0^4 / (2r^2) + v_z^2 / 2$ are the dynamic pressures, and ρgz is the potential pressure. If $r \geq r_0$, referring to the boundary conditions: $z|_{r \rightarrow \infty} = v|_{r \rightarrow \infty} = v_z|_{r \rightarrow \infty} = 0$, $p|_{r \rightarrow \infty} = P_0$, then $C_2 = 0$. If $r \leq r_0$, $p|_{r \geq r_0, r=r_0} = p|_{r \leq r_0, r=r_0}$, then $C_1 = 0$, and Eq. (5) is transformed as

$$p(r, z) = \begin{cases} P_0 + \rho gz - \frac{1}{2} v_z^2 - \rho r_0^2 \omega^2 \left(1 - \frac{r^2}{2r_0^2} \right), & r \leq r_0, \\ P_0 + \rho gz - \frac{1}{2} v_z^2 - \frac{\rho \omega^2 r_0^4}{2r^2}, & r \geq r_0. \end{cases} \quad (7)$$

3 Helmholtz-equation-based solution method

As indicated above, the critical penetration condition of a sink vortex was the key research target of this study. To address the issue, we propose a Helmholtz-equation-based solution method.

Firstly, the mathematical expression for the axial velocity at the critical penetration state should be obtained. If $r=0$, the free surface height is at its minimum, i.e. the maximum of the vortex depth. In the vortex penetration process, the vortex depth increases monotonously, then $v_z = \partial z / \partial t > 0$, but it is hard to obtain the explicit relations among the vortex physical parameters. As the vortex depth increases, the fluid pressure of the vortex core will reduce continuously, i.e. $\partial p / \partial z < 0$, which is a necessary condition for the free surface to descend. Any one point of the vortex core surface can satisfy the above condition. Therefore, taking the $r=0$ point as the research object, we can obtain:

$$\left. \frac{\partial p}{\partial z} \right|_{r=0} = \left(\rho g - \rho v_z \frac{\partial v_z}{\partial z} - 2\rho \omega r_0^2 \frac{\partial \omega}{\partial z} \right) \Big|_{r=0} < 0. \quad (8)$$

Then, let Eq. (2) embed into the Helmholtz equation (Matsumoto and Hoshino, 2004; Basu et al., 2012):

$$\begin{aligned} \frac{\partial \Omega}{\partial t} + (\mathbf{v} \cdot \nabla) \Omega &= (\Omega \cdot \nabla) \mathbf{v} + \nu \nabla^2 \Omega, \\ \Rightarrow \frac{\partial \omega_i}{\partial t} + v_j \frac{\partial \omega_i}{\partial x_j} &= \omega_i \frac{\partial v_j}{\partial x_j} + \nu \frac{\partial^2 \omega_i}{\partial x_i \partial x_j}, \end{aligned} \quad (9)$$

where ν is the fluid kinematic viscosity. Considering the vortex penetration process, the motion laws of the vortex core fluid are unsteady. Therefore, we take the fluid that is at the critical time point of vortex penetration as the research object, and solve the critical condition of vortex penetration. In the above hypothesis, the fluid of the vortex core can be regarded as a steady inviscid flow. If the effects of time-varying parameters and viscosity are ignored, the following expression is obtained:

$$v_z \frac{\partial \omega}{\partial z} = \omega \frac{\partial v_z}{\partial z} \Rightarrow \frac{\partial \omega}{\partial z} = \frac{\omega}{v_z} \frac{\partial v_z}{\partial z}. \quad (10)$$

Substituting Eq. (10) into Eq. (8), we can obtain:

$$\begin{aligned} \left. \frac{\partial p}{\partial z} \right|_{r=0} &= \rho \left(g - v_z \frac{\partial v_z}{\partial z} - 2r_0^2 \omega \frac{\partial v_z}{v_z \partial z} \right) \\ &= \rho \left[g - \frac{\partial v_z}{\partial z} \left(v_z + \frac{2\omega^2 r_0^2}{v_z} \right) \right] \\ &= \rho \left[g - \frac{\partial v_z}{\partial z} \left(v_z + \frac{\Gamma^2}{2\pi^2 r_0^2} \frac{1}{v_z} \right) \right]. \end{aligned} \quad (11)$$

The critical condition of vortex penetration is

$$\frac{\partial v_z}{\partial z} \left(v_z + \frac{\Gamma^2}{2\pi^2 r_0^2} \frac{1}{v_z} \right) = g. \quad (12)$$

Finally, Eq. (12) is integrated by the variable separation method, and the vortex depth can be described as

$$z = Av_z^2 + B \ln v_z + C_3, \quad (13)$$

where $A = 1/(2g)$, $B = 2r_0^2 \omega^2 / g$. Referring to the boundary condition: $v_z|_{z=0} = 0$, then $C_3 = -2r_0^2 \omega^2 / g$, and Eq. (13) is transformed as

$$z = Av_z^2 + B(\ln v_z - 1). \quad (14)$$

The above transcendental equation is the mathematical expression of axial velocity and depth for the vortex penetration process.

According to Eq. (14), we infer that the axial disturbing velocity v_z has an important effect on vortex formation, and has the same monotone increasing trend as z , i.e. $\partial v_z / \partial z > 0$. At the time point of vortex penetration, v_z will be at the maximum amplitude. During the course of drainage, v_z and z depend directly on the flow quantity. With increasing flow quantity, the vorticity intensity Γ and angular velocity ω increase, and v_z will have larger amplitude. Therefore, changing the flow quantity is an effective measure to control the vortex formation process.

4 Numerical results and discussion

4.1 Critical penetration condition

To obtain numerical results from the proposed method, a numerical model of a sink vortex was set up, with the boundary conditions listed in Table 1.

Table 1 Boundary conditions of the vortex numerical model

Item	Attribute
Inlet	Pressure inlet
Outlet	Pressure outlet
Wall	Rotating wall
Reference pressure (Pa)	1.01×10^5
Zone	Air, water
Vessel height (m)	0.5
Vessel diameter (m)	0.2
Pipe length (m)	0.1

The flow field is affected by the Coriolis acceleration and initial disturbance velocity (ω_0), so the simulation of the free vortex formation process should consider the influences of different initial rotating velocities. We considered three groups of rotating velocities: 1.5π rad/s, 2.0π rad/s, and 3.0π rad/s, with the corresponding Reynolds numbers 12000, 16000, and 24000, respectively, in which the turbulence state will be formed (Ji et al., 2010, 2012; Turkyilmazoglu, 2011; Tan et al., 2016b; Qi et al., 2017; Nguyen et al., 2018).

Since sink vortex evolution is typically an unsteady process, the simulation needs to address the

transition flow with complex inter-phase variations (Zheng et al., 2012; Zhang et al., 2018a). The coupling processing for pressure and velocity is conducted by the pressure implicit with splitting of operators (PISO) algorithm to guarantee convergence efficiency. By the pressure staggering option (PRESTO) method, discrete pressure interpolation is performed to avoid higher fluctuation of internal pressure. The momentum and rotating velocity adopt the second-order upwind to obtain a precise solution (Li et al., 2012, 2013; Tan et al., 2017a; Qi et al., 2018; Zhang et al., 2018b; Zhang LB et al., 2018).

To verify the validity of Eq. (14), a numerical instance is provided and an observation experiment was conducted. The results are shown in Fig. 3. The initial rotating velocity is 2π rad/s. The dashed line is a critical condition set of vortex penetration, and describes the relation between the effects of v_z and z on the critical state of vortex penetration. Therefore, in the upper zone of the curve, the rotation energy would break through the surface tension, and the vortex would enter the penetration state. For the primary stage of vortex formation ($z_1=0.07$ m), v_z shows apparent fluctuation caused by the velocity ascending process of the servo motor of the experimental apparatus. Then, the experimental curve is near to the theoretical curve. For the fluid viscosity resistance, the actual velocity amplitude is less than the theoretical value ($z_2=0.09$ m), and W can be regarded as the viscosity work, as shown in the shaded area in Fig. 3.

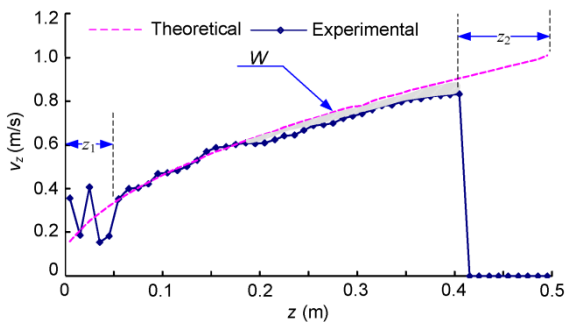


Fig. 3 Curve of vortex height and axial velocity

The radial velocity profiles of the sink vortex were obtained (Fig. 4). For the two velocity curves of the air phase, there are apparent upwelling phenomena caused by Ekman boundary coupling effects. The three liquid phase curves take on characteristics of a

Rankine vortex, and the control region of the vortex is within the radial range of 0–0.08 m. With increasing radial distance, all the velocity curves tend to zero, which represents the balanced state of circumferential velocity, inertial force, and viscous resistance.

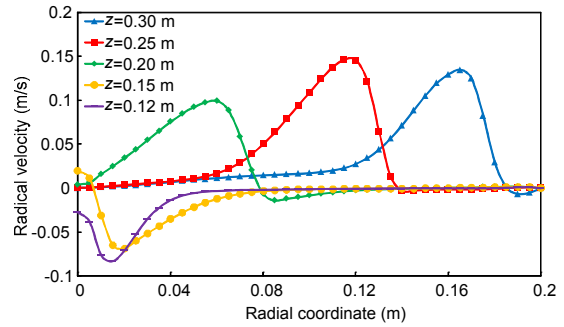


Fig. 4 Radial velocity profiles

The curves of $z=0.30$ m, $z=0.25$ m, and $z=0.20$ m are velocity profiles of the liquid phase, and the curves of $z=0.15$ m and $z=0.12$ m are the profiles of the air phase

4.2 Suction-extraction of Ekman boundary layer

For the Ekman suction-extraction mechanism of a sink vortex, two numerical instances were considered in which the penetration state is divided into two stages: suction and extraction. The gas-liquid volume fractions in the vortex suction stage at different rotating velocities are shown in Fig. 5, in which the air zone is marked red, and the water zone blue. The bottom point of the liquid surface is the position of the suction hole, and the inter-phase coupling zone marked green is the boundary layer.

To reveal the regularities of Ekman boundary layer coupling, the stream line profiles of the suction stage were acquired (Fig. 6). (1) In the suction hole, a small quantity of air is sucked into the liquid and transmitted to the drainage pipe, and most of air flow is back along the tangential direction of the liquid surface. (2) The central point of the suction hole is at the minimum height of the liquid surface, which keeps a constant value owing to the variation in circumferential velocity. (3) In the liquid boundary layer, there is an apparent upwelling caused by Ekman spiral coupling effects. (4) The thickness of the Ekman layer is related to the circumferential velocity. If the circumferential velocity becomes larger, the macro-combination of turbulence vortices will lead to higher transportation efficiency. The above effects which can make small-scale vortices have larger

velocity gradients and viscous stress, so the thickness of the boundary layer will be increased.

With the evolution of the suction process, the increasing vortex energy can cause more air to be

sucked into the subsurface, forming bubbles with larger sizes. This is the vortex extraction stage. The stream line profiles of the extraction stage are shown in Fig. 7. (1) Owing to the viscous resistance of the

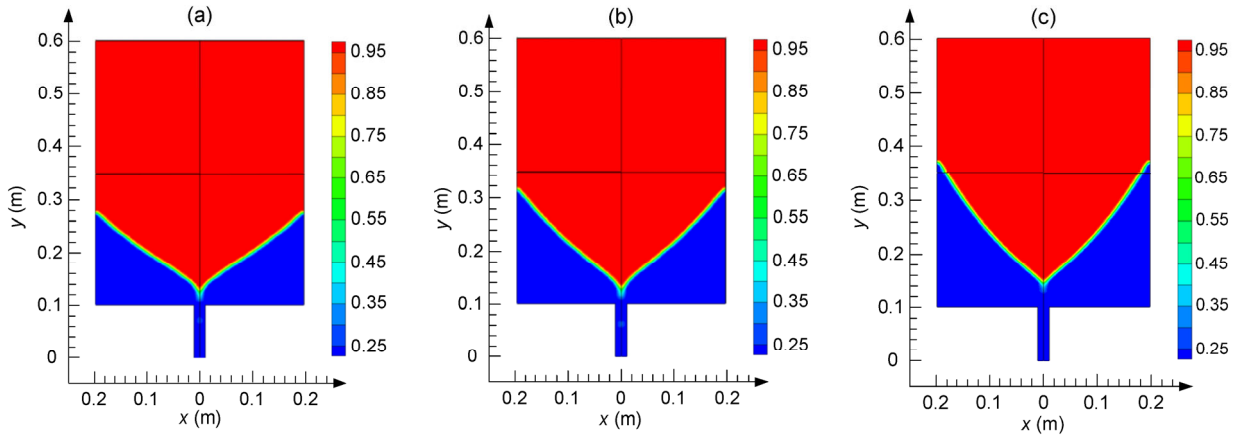


Fig. 5 Two-phase fractions in the suction stage

(a) $\omega_0=1.5\pi$ rad/s, $t=27.00$ s; (b) $\omega_0=2\pi$ rad/s, $t=22.40$ s; (c) $\omega_0=3\pi$ rad/s, $t=16.00$ s

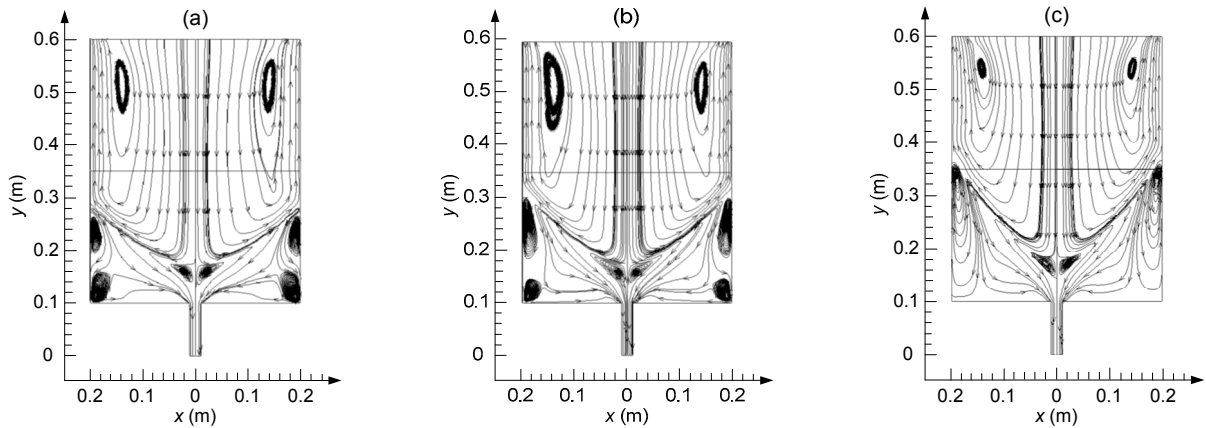


Fig. 6 Stream lines of the suction stage

(a) $\omega_0=1.5\pi$ rad/s, $t=27.00$ s; (b) $\omega_0=2\pi$ rad/s, $t=22.40$ s; (c) $\omega_0=3\pi$ rad/s, $t=16.00$ s

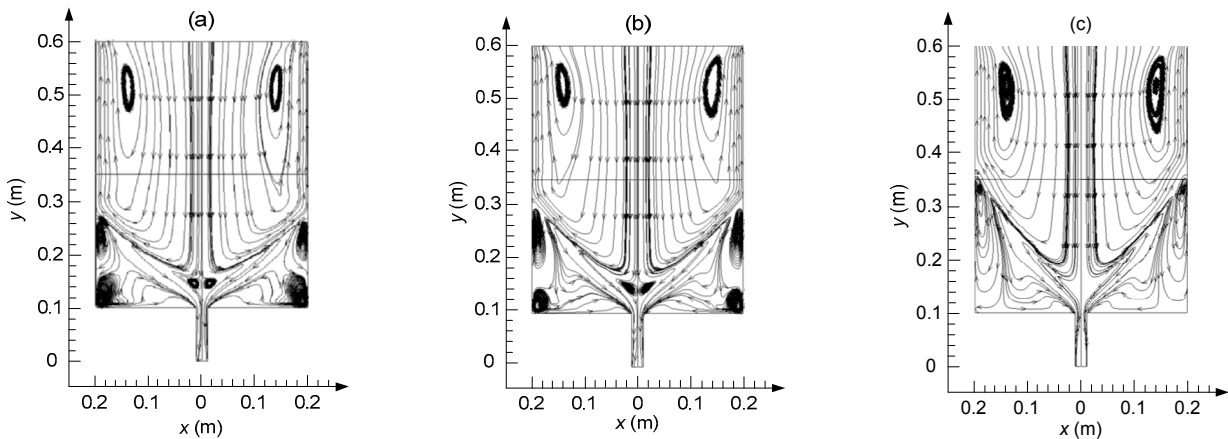


Fig. 7 Stream lines of the extraction stage

(a) $\omega_0=1.5\pi$ rad/s, $t=29.50$ s; (b) $\omega_0=2\pi$ rad/s, $t=25.00$ s; (c) $\omega_0=3\pi$ rad/s, $t=20.08$ s

Ekman layer, the horizontal velocity decreases, and the dynamical pressure of vertical vortices will reduce. (2) As the circumferential component increases, the Reynolds number and turbulence intensity will be enhanced. This can expand the effecting range of boundary layer vortices. (3) The external potential flow can embed deeply into the boundary layer, and the surface between turbulence and potential flow takes on an unstable state. Accordingly, the external layer thickness of the boundary layer becomes larger, the thickness of the viscous layer decreases, and the Ekman extraction phenomena will disappear.

5 Observational experiments

To verify the numerical results, we set up a particle image velocimetry (PIV) experimental platform to observe the vortex penetration process (Fig. 8). To obtain the precise detailed features of the sink vortex, a binocular endoscope was adopted to capture the real-time vortex image. A sink vortex generation device was constructed to provide the required vortex in the measurement range of the endoscope. The vortex generation device contained a transparent shell to observe the vortex, and a servo motor to generate the required rotation velocity. Moreover, the platform contained a high frequency laser to generate ultra-fast pulses, and a post-processing system to obtain the velocity vector and vorticity contour.

The experimental conditions were as follows. The environment temperature was 24 °C. Water was poured into the vessel, and stood for 30 min. Micro polypropylene particles were selected as the tracing particles (Di et al., 2015; Zeng et al., 2016; Zheng et al., 2017). The average diameter of the particles was 5 μm, and their density was 0.95 g/cm³. The PIV capture frequency was 7.4 Hz.

Based on the PIV platform, the observational results of the vortex penetration process are shown in Fig. 9 and Fig. 10 (p.69). (1) The vortex core boundary was observed (Figs. 9a–9c and Figs. 10a–10c), so the radius of the vortex core could be acquired. This was important for improving the effectiveness of the theoretical vortex models. (2) As the circumferential component increased, the vortex depth remained constant in a formation state (suction or extraction).

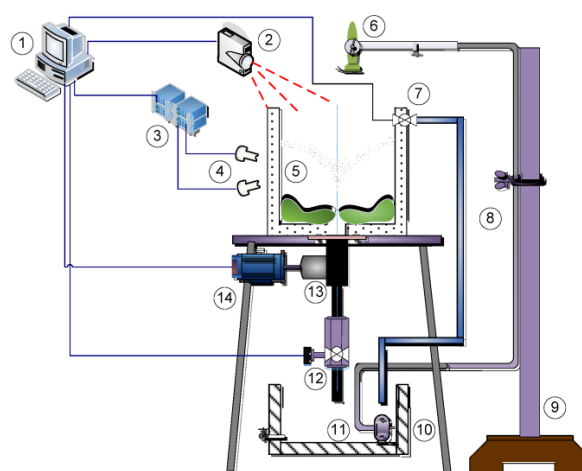


Fig. 8 Schematic diagram of PIV observational experiment platform

1: post-processing system; 2: high-frequency pulse laser; 3: PIV apparatus; 4: double pipe endoscope; 5: cylindrical vessel; 6: pouring apparatus; 7: overflow valve; 8: polyvinyl chloride (PVC) soft pipe; 9: angle-steel supporter; 10: micro submersible pump; 11: rectangular vessel; 12: drainage pipe; 13: mechanical drive apparatus; 14: servo motor

(3) There was an Ekman upwelling of fluid near the vortex surface in the suction stage (Figs. 9d–9f). Moreover, as the velocity increased, the Ekman suction intensity increased. The above results accord with the simulated results (Fig. 6), as well as the experimental results of Andersen et al. (2003, 2006). (4) In the vortex extraction stage, the surface fluid displayed the Ekman pumping phenomenon (Figs. 10d–10f) in accord with the simulated results (Fig. 7). However, as the circumferential velocity increased, the pumping intensity tended to decline. (5) At the front-end area of the vortex in the suction stage, the vorticity showed an aggregation trend (Figs. 9g–9i), revealing the transition process from potential to kinetic energy. (6) At the front-end area in the extraction stage, the vorticity decreased as the velocity increased (Figs. 10g–10i). This proved that the vortex was in the complete penetration stage, in which it has the maximum kinetic energy. The energy then dissipated gradually until the vortex disappeared.

6 Conclusions

The formation mechanism and active control of sink vortices have important scientific significance

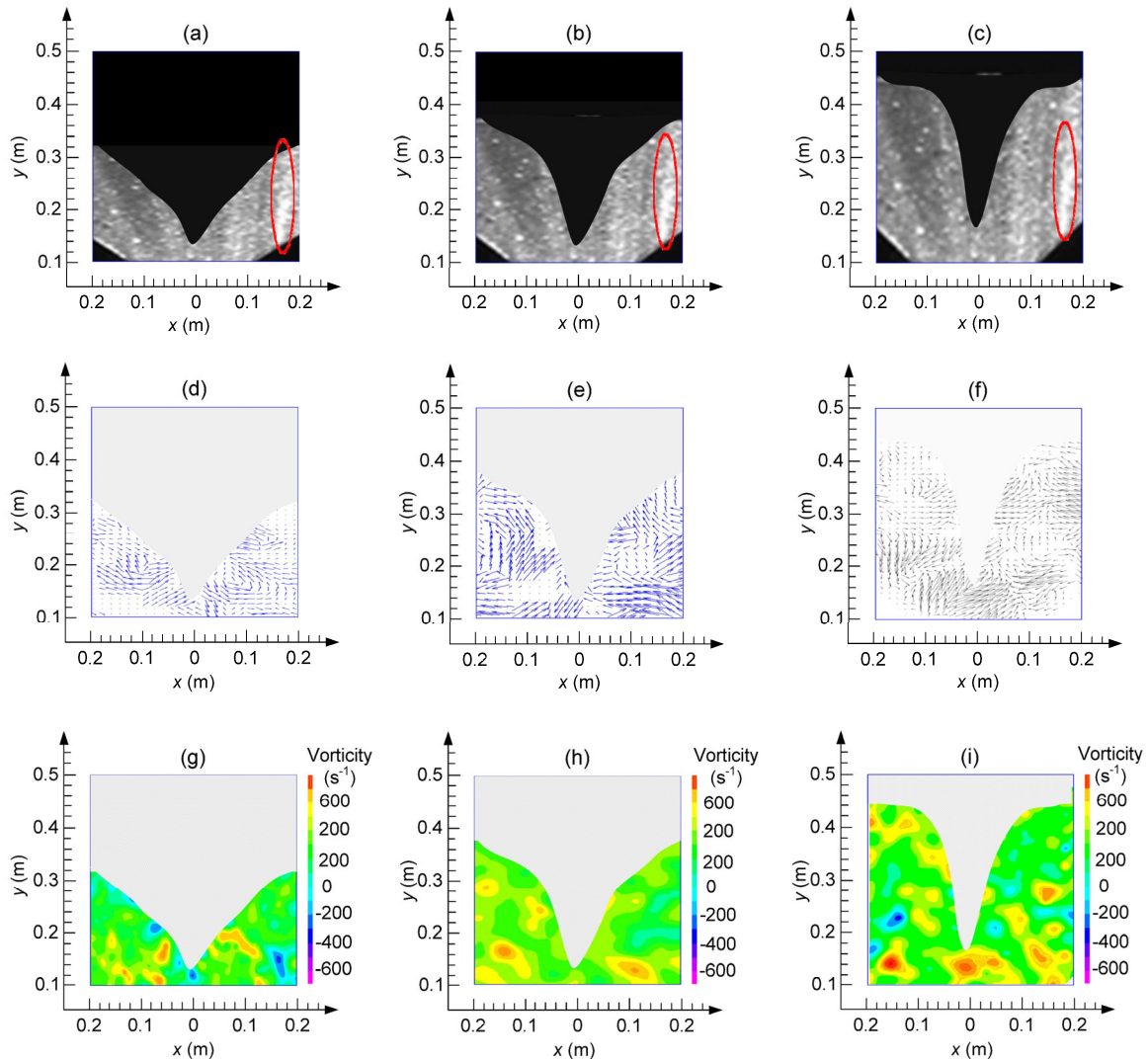


Fig. 9 PIV results of suction stage at three initial rotating velocities (1.5π rad/s, 2π rad/s, and 3π rad/s)

(a)-(c) PIV photos: the highlight zone is the boundary of the vortex (incoming flow direction), where the fluid has the maximum linear velocity; (d)-(f) Velocity vectors: the velocity vector near to vortex surface points to the up direction, and it is the effect of Ekman suction; (g)-(i) Vorticity profiles: the fluid vorticity is aggregating at the vortex end, reflecting a transition process of turbulent kinetic energy

for some engineering applications. To address this issue, we presented an analytical sink vortex mechanical model to obtain the critical condition of vortex formation, and reveal Ekman boundary layer suction-extraction regularities in the vortex penetration process. Appropriate experiments were performed to validate the model. The main conclusions are as follows.

A Rankine-vortex-based fluid mechanic model was set up to obtain the fundamental velocity/pressure profiles of a sink vortex. A Helmholtz-

equation-based solution method was proposed to acquire the critical penetration condition of a sink vortex. Based on the above model and solution method, the Ekman boundary layer suction-extraction laws were revealed. Numerical results showed that the critical penetration condition of a sink vortex contains multiple solutions depending on the initial flow field states; the heights of suction/extraction holes from the container bottom are determined by geometrical parameters, and are not related to the initial velocity components; if the initial disturbances

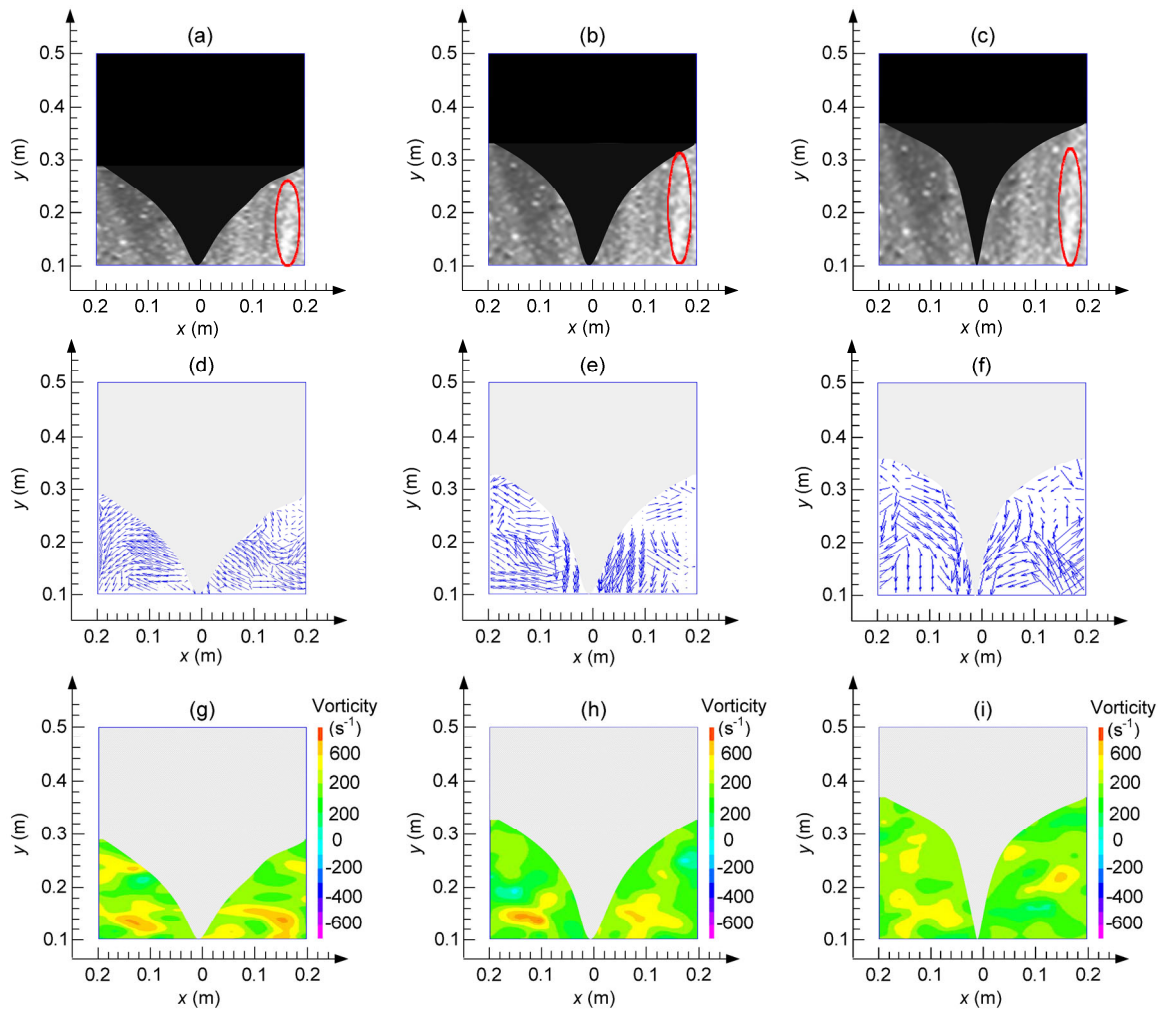


Fig. 10 PIV results of extraction stage at three initial rotating velocities (1.5π rad/s, 2π rad/s, and 3π rad/s)

(a)-(c) PIV photos: on the incoming flow direction, the vortex boundaries can be observed; (d)-(f) Velocity vectors: for the vortex surface region, there is an upstream caused by Ekman extraction; (g)-(i) Vorticity profiles: the fluid vorticity tends to be lower, which reflects the energy dissipation process of the vortex

are enhanced, the suction-extraction height and Ekman layer thickness increase, but the Ekman boundary vorticity intensities of the two stages (suction, extraction) decline.

A PIV observation experimental platform was established, and the effectiveness of the proposed model and solution method was verified. Moreover, using the PIV experimental platform, we observed the vortex core radius and vorticity aggregation. The vortex core radius is a key parameter for all theoretical vortex models, and is commonly acquired by the experimental data regression method. The above result is important for improving the effectiveness of theoretical vortex models.

The proposed methods can provide direct guidance for the active control of sink vortex formation, and technical evidence for related engineering areas. Subsequent studies will explore facets of the finite element method-discrete element method (FEM-DEM) coupled solution for a multi-phase vortex and the vibration shock characteristics of the penetration process.

References

- Aboelkassem Y, Georgicis V, 2007. New model for compressible vortices. *ASME Journal of Fluids Engineering*, 129(8):1073-1079.
<https://doi.org/10.1115/1.2746897>

- Aboelkassem Y, Vattistas GH, Esmail N, 2005. Viscous dissipation of Rankine vortex profile in zero meridional flow. *Acta Mechanica Sinica*, 21(6):550-556.
<https://doi.org/10.1007/s10409-005-0073-3>
- Andersen A, Bohr T, Stenum B, 2003. Anatomy of a bathtub vortex. *Physical Review Letters*, 91(10):104502.
<https://doi.org/10.1103/PhysRevLett.91.104502>
- Andersen A, Bohr T, Stenum B, 2006. The bathtub vortex in a rotating container. *Journal of Fluid Mechanics*, 556:121-146.
<https://doi.org/10.1017/S0022112006009463>
- Basu S, Saha A, Kumar R, 2012. Thermally induced secondary atomization of droplet in an acoustic field. *Applied Physics Letters*, 100(5):054101.
<https://doi.org/10.1063/1.3680257>
- Chen JL, Xu F, Tan DP, et al., 2015. A control method for agricultural greenhouses heating based on computational fluid dynamics and energy prediction model. *Applied Energy*, 141:106-118.
<https://doi.org/10.1016/j.apenergy.2014.12.026>
- Chen YC, Huang SL, Li ZY, et al., 2013. A bathtub vortex under the influence of a protruding cylinder in a rotating tank. *Journal of Fluid Mechanics*, 733:134-157.
<https://doi.org/10.1017/jfm.2013.441>
- Chen ST, Tan DP, 2018. A SA-ANN-based modeling method for human cognition mechanism and the PSACO cognition algorithm. *Complexity*, 2018:6264124.
<https://doi.org/10.1155/2018/6264124>
- Di J, Fu XC, Zheng HJ, et al., 2015. H-TiO₂/C/MnO₂ nanocomposite materials for high-performance supercapacitors. *Journal of Nanoparticle Research*, 17(6):255.
<https://doi.org/10.1007/s11051-015-3060-z>
- Ding H, Lv JD, Wu HP, et al., 2018. Enhanced light-harvesting by plasmonic hollow gold nanospheres for photovoltaic performance. *Royal Society Open Science*, 5(1):171350.
<https://doi.org/10.1098/rsos.171350>
- Dolan SR, Oliveira ES, 2013. Scattering by a draining bathtub vortex. *Physical Review D*, 87(12):124038.
<https://doi.org/10.1103/PhysRevD.87.124038>
- Ge JQ, Tan DP, Ji SM, 2018. A gas-liquid-solid three-phase abrasive flow processing method based on bubble collapsing. *International Journal of Advanced Manufacturing Technology*, 95(1-4):1069-1085.
<https://doi.org/10.1007/s00170-017-1250-9>
- Ghani IA, Sidik NAC, Kamaruzaman N, 2017. Hydrothermal performance of microchannel heat sink: the effect of channel design. *International Journal of Heat and Mass Transfer*, 107:21-44.
<https://doi.org/10.1016/j.ijheatmasstransfer.2016.11.031>
- Huang XY, Cheng WJ, Zhong W, et al., 2017. Development of new pressure regulator with flowrate-amplification using vacuum ejector. *Vacuum*, 144:172-182.
<https://doi.org/10.1016/j.precisioneng.2018.01.006>
- Ji SM, Xiao FQ, Tan DP, 2010. Analytical method for softness abrasive flow field based on discrete phase model. *Science China-Technological Sciences*, 53(10):2867-2877.
<https://doi.org/10.1007/s11431-010-4046-9>
- Ji SM, Weng XX, Tan DP, 2012. Analytical method of softness abrasive two-phase flow field based on 2D model of LSM. *Acta Physica Sinica*, 61(1):010205 (in Chinese).
- Ji SM, Ge JQ, Tan DP, 2017. Wall contact effects of particle-wall collision process in two-phase particle fluid. *Journal of Zhejiang University-SCIENCE A (Applied Physics & Engineering)*, 18(12):958-973.
<https://doi.org/10.1631/jzus.A1700039>
- Li C, Ji SM, Tan DP, 2012. Softness abrasive flow method oriented to tiny scale mold structural surface. *International Journal of Advanced Manufacturing Technology*, 61(9-12):975-987.
<https://doi.org/10.1007/s00170-011-3621-y>
- Li C, Ji SM, Tan DP, 2013. Multiple-loop digital control method for 400 Hz inverter system based on phase feedback. *IEEE Transactions on Power Electronics*, 28(1):408-417.
<https://doi.org/10.1109/TPEL.2012.2188043>
- Li HX, Wang Q, Jiang J, et al., 2016. Analysis of factors affecting free surface vortex formation during steel teeming. *ISIJ International*, 56(1):94-102.
<https://doi.org/10.2355/isijinternational.ISIJINT-2015-096>
- Li J, Ji SM, Tan DP, 2017. Improved soft abrasive flow finishing method based on turbulent kinetic energy enhancing. *Chinese Journal of Mechanical Engineering*, 30(2):301-309.
<https://doi.org/10.1007/s10033-017-0071-y>
- Li PX, Liu P, Liu ZC, et al., 2017. Experimental and numerical study on the heat transfer and flow performance for the circular tube fitted with drainage inserts. *International Journal of Heat and Mass Transfer*, 107:686-696.
<https://doi.org/10.1016/j.ijheatmasstransfer.2016.11.094>
- Lin R, Yan ZG, Yu JK, 2010. Physical modeling test of vortex during teeming from ladle. *Journal of Northeastern University*, 31(9):1287-1291.
- Lundgren TS, 1985. The vortical flow above the drain-hole in a rotating vessel. *Journal of Fluid Mechanics*, 155:381-412.
<https://doi.org/10.1017/S0022112085001860>
- Matsumoto Y, Hoshino M, 2004. Onset of turbulence induced by a Kelvin-Helmholtz vortex. *Geophysical Research Letters*, 31(2):L02807.
<https://doi.org/10.1029/2003GL018195>
- Nguyen T, Liu D, Thongkaew K, et al., 2018. The wear mechanisms of reaction bonded silicon carbide under abrasive polishing and slurry jet impact conditions. *Wear*, 410-411:156-164.
<https://doi.org/10.1016/j.wear.2018.06.001>
- Peterson SD, Porfiri M, 2012. Energy exchange between a vortex ring and an ionic polymer metal composite. *Applied Physics Letters*, 100(11):114102.
<https://doi.org/10.1063/1.3693184>
- Qi H, Xie Z, Hong T, et al., 2017. CFD modelling of a novel hydrodynamic suspension polishing process for ultra-smooth surface with low residual stress. *Powder*

- Technology, 317:320-328.
<https://doi.org/10.1016/j.powtec.2017.05.030>
- Qi H, Cheng Z, Cai D, et al., 2018. Experimental study on the improvement of surface integrity of tungsten steel using acoustic levitation polishing. *Journal of Materials Processing Technology*, 259:361-367.
<https://doi.org/10.1016/j.jmatprotec.2018.04.043>
- Shi KG, Li X, 2018. Experimental and theoretical study of dynamic characteristics of Bernoulli gripper. *Precision Engineering*, 52:323-331.
<https://doi.org/10.1016/j.precisioneng.2018.01.006>
- Shi YX, Fox RO, Olsen MG, 2011. Confocal imaging of laminar and turbulent mixing in a microscale multi-inlet vortex nanoprecipitation reactor. *Applied Physics Letters*, 99(20):204103.
<https://doi.org/10.1063/1.3662042>
- Tan DP, Zhang LB, 2014. A WP-based nonlinear vibration sensing method for invisible liquid steel slag detection. *Sensors and Actuators B-Chemical*, 202:1257-1269.
<https://doi.org/10.1016/j.snb.2014.06.014>
- Tan DP, Li PY, Pan XH, 2009. Application of improved HMM algorithm in slag detection system. *Journal of Iron and Steel Research International*, 16(1):1-6.
[https://doi.org/10.1016/S1006-706X\(09\)60001-7](https://doi.org/10.1016/S1006-706X(09)60001-7)
- Tan DP, Ji SM, Li PY, et al., 2010. Development of vibration style ladle slag detection method and the key technologies. *Science China-Technological Sciences*, 53(9):2378-2387.
<https://doi.org/10.1007/s11431-010-4073-6>
- Tan DP, Li PY, Ji YX, et al., 2013. SA-ANN-based slag carry-over detection method and the embedded WME platform. *IEEE Transactions on Industrial Electronics*, 60(10):4702-4713.
<https://doi.org/10.1109/TIE.2012.2213559>
- Tan DP, Zhang LB, Ai QL, 2016a. An embedded self-adapting network service framework for networked manufacturing system. *Journal Intelligent Manufacturing*, p.1-18.
<https://doi.org/10.1007/s10845-016-1265-3>
- Tan DP, Yang T, Zhao J, et al., 2016b. Free sink vortex Ekman suction-extraction evolution mechanism. *Acta Physica Sinica*, 65(5):054701.
<https://doi.org/10.7498/aps.65.054701>
- Tan DP, Ji SM, Fu YZ, 2016c. An improved soft abrasive flow finishing method based on fluid collision theory. *International Journal of Advanced Manufacturing Technology*, 85(5-8):1261-1274.
<https://doi.org/10.1007/s00170-015-8044-8>
- Tan DP, Li L, Zhu YL, et al., 2017a. An embedded cloud database service method for distributed industry monitoring. *IEEE Transactions on Industrial Informatics*, 14(7):2881-2893.
<https://doi.org/10.1109/TII.2017.2773644>
- Tan DP, Chen ST, Bao GJ, et al., 2017b. An embedded lightweight GUI component library and the ergonomics optimization method for industry process monitoring. *Frontiers of Information Technology & Electronic Engineering*, 19(5):604-625.
<https://doi.org/10.1631/FITEE.1601660>
- Tan DP, Ni YS, Zhang LB, 2017c. Two-phase sink vortex suction mechanism and penetration dynamic characteristics in ladle teeming process. *Journal of Iron and Steel Research International*, 24(7):669-677.
[https://doi.org/10.1016/S1006-706X\(17\)30101-2](https://doi.org/10.1016/S1006-706X(17)30101-2)
- Tong SP, 2006. *Advanced Fluid Mechanics*. China University of Petroleum Press, Dongying, China, p.155 (in Chinese).
- Turkylmazoglu M, 2011. Wall stretching in magnetohydrodynamics rotating flows in inertial and rotating frames. *Journal of Thermophysics and Heat Transfer*, 25(4):606-613.
<https://doi.org/10.2514/1.T3750>
- Turkylmazoglu M, 2018. Flow and heat due to a surface formed by a vortical source. *European Journal of Mechanics B-Fluids*, 68:76-84.
<https://doi.org/10.1016/j.euromechflu.2017.11.010>
- Tyvand PA, Haugena KB, 2005. An impulsive bathtub vortex. *Physics of Fluids*, 17:062105.
<https://doi.org/10.1063/1.1938216>
- Wang XH, Liu AP, Xing Y, et al., 2018. Three-dimensional graphene biointerface with extremely high sensitivity to single cancer cell monitoring. *Biosensors & Bioelectronics*, 105:22-28.
<https://doi.org/10.1016/j.bios.2018.01.012>
- Wu HP, Li L, Chai GZ, et al., 2016. Three-dimensional thermal weight function method for the interface crack problems in bimaterial structures under a transient thermal loading. *Journal of Thermal Stresses*, 39(4):371-385.
<https://doi.org/10.1080/01495739.2016.1152108>
- Wu ZH, Zheng NG, Zhang SW, et al., 2016. Maze learning by a hybrid brain-computer system. *Scientific Reports*, 6:31746.
<https://doi.org/10.1038/srep31746>
- Yokoyama N, Maruyama Y, Mizushima J, 2012. Origin of the bathtub vortex and its formation mechanism. *Journal of the Physical Society of Japan*, 81(7):074401.
<https://doi.org/10.1143/JPSJ.81.074401>
- Zeng X, Ji SM, Tan DP, et al., 2013. Softness consolidation abrasives material removal characteristic oriented to laser hardening surface. *International Journal of Advanced Manufacturing Technology*, 69(9-12):2323-2332.
<https://doi.org/10.1007/s00170-013-4985-y>
- Zeng X, Ji SM, Jin MS, et al., 2014. Investigation on machining characteristic of pneumatic wheel based on softness consolidation abrasives. *International Journal of Precision Engineering and Manufacturing*, 15(10):2031-2039.
<https://doi.org/10.1007/s12541-014-0560-1>
- Zeng X, Ji SM, Jin MS, et al., 2016. Research on dynamic characteristic of softness consolidation abrasives in machining process. *International Journal of Advanced Manufacturing Technology*, 82(5-8):1115-1125.

- <https://doi.org/10.1007/s00170-015-7392-8>
Zhang L, Wang JS, Tan DP, et al., 2017. Gas compensation based abrasive flow processing method for complex titanium alloy surfaces. *International Journal of Advanced Manufacturing Technology*, 92(9-12):3385-3397.
<https://doi.org/10.1007/s00170-017-0400-4>
- Zhang L, Yuan Z, Qi Z, et al., 2018a. CFD-based study of the abrasive flow characteristics within constrained flow passage in polishing of complex titanium alloy surfaces. *Powder Technology*, 333:209-218.
<https://doi.org/10.1016/j.powtec.2018.04.046>
- Zhang L, Yuan Z, Tan DP, et al., 2018b. An improved abrasive flow processing method for complex geometric surfaces of titanium alloy artificial joints. *Applied Sciences*, 8(7):1037.
<https://doi.org/10.3390/app8071037>
- Zhang LB, Lv HP, Tan DP, et al., 2018. An adaptive quantum genetic algorithm for task sequence planning of complex assembly systems. *Electronics Letters*, 54(14):870-872.
<https://doi.org/10.1049/el.2018.0609>
- Zhao JH, Li X, 2016. Effect of supply flow rate on performance of pneumatic non-contact gripper using vortex flow. *Experimental Thermal and Fluid Science*, 79:91-100.
<https://doi.org/10.1016/j.expthermflusci.2016.06.020>
- Zhao ZF, Zhou H, Zheng LX, et al., 2017. Molecules interface engineering derived external electric field for effective charge separation in photoelectrocatalysis. *Nano Energy*, 42:90-97.
<https://doi.org/10.1007/s00170-015-7392-8>
- Zheng HJ, Wang JX, Jia Y, et al., 2012. In-situ synthesize multi-walled carbon nanotubes@MnO₂ nanoflake core-shell structured materials for supercapacitors. *Journal of Power Sources*, 216:508-514.
<https://doi.org/10.1016/j.jpowsour.2012.06.047>
- Zheng HJ, Niu P, Zhao ZF, 2017. Carbon quantum dot sensitized Pt@Bi₂WO₆/FTO electrodes for enhanced photoelectro-catalytic activity of methanol oxidation. *RCS Advances*, 7(43):26943-26951.
<https://doi.org/10.1039/c7ra01867c>

- Zheng NG, Su LJ, Zhang DQ, et al., 2015. A computational model for ratbot locomotion based on cyborg intelligence. *Neurocomputing*, 170:92-97.
<https://doi.org/10.1016/j.neucom.2014.12.115>

中文概要

题目: 汇流旋涡临界贯穿条件与 Ekman 抽吸演化机理

目的: 提出一种自由汇流旋涡形成过程建模求解方法, 得到其临界贯穿条件, 并揭示其 Ekman 边界层抽吸演化机理。

创新点: 1. 基于二维 Rankine 位势涡理论, 建立自由汇流旋涡动力学模型, 得到其压力、速度分布; 2. 提出一种基于 Helmholtz 方程的汇流旋涡贯穿临界条件求解方法; 3. 成功搭建一种基于双目内窥技术的汇流旋涡观测实验平台, 可实现对旋涡贯穿及 Ekman 抽吸过程的精确观测。

方法: 1. 将汇流旋涡定义为涡核与核外流两部分, 并基于 Bernoulli 方程与 Lamb-ΓPOMEKO 方程得到汇流旋涡界面形状及压力、速度分布; 2. 基于上述动力学模型, 结合 Helmholtz 涡量动力学方程, 利用分离变量积分方法, 得到旋涡形成轴向速度与深度的解析关系表达式; 3. 基于粒子图像测速 (PIV) 方法, 结合双目内窥技术, 实现对汇流旋涡临界贯穿与边界层抽吸的流动细节特征的实时追踪。

结论: 1. 汇流旋涡临界贯穿条件是一个解集, 这是由不同的流场初始扰动条件造成的; 2. 旋涡抽吸孔最低点的高度由容器的几何参数决定, 与初始扰动速度无关; 3. 若初始扰动增强, 旋涡深度与 Ekman 层厚度增加, 但在抽吸过程中的边界层涡量强度有减弱趋势; 4. PIV 实验验证了上述理论结果的正确性, 并观测到旋涡半径边界与涡量集聚现象。

关键词: 汇流旋涡; 临界贯穿条件; Ekman 边界层; 抽吸演化机理